American Welding Society®

SUPPLEMENT TO THE *WELDING JOURNAL*, JULY 2022
Sponsored by the American Welding Society

WELDING RESEARCH

Narrow Groove Laser-Arc Hybrid Welding of Thick-Sectioned HSLA Steel Using Laser Beam Oscillation

The use of an oscillated laser beam to suppress the incomplete fusion phenomenon and improve the process stability of NGHW was proposed

BY Y. WU, Z. LI, X. WANG, Y. FENG, M. WANG, AND J. SHAN

Abstract

In this study, a sine-oscillating laser was used to obtain narrow groove laser-arc hybrid welding (NGHW) of high-strength low-alloy (HSLA) steel. Then the effects of laser beam oscillation amplitude and space constraint on arc behavior, droplet transfer, weld geometry, and incomplete fusion of the weld beads were analyzed. Due to the minimum arc voltage principle and inherent arc self-regulation, when the laser did not oscillate, it was observed that the arc cathode spot was typically attached to one sidewall. As a result, the molten pool did not spread through the entire width of the gap, resulting in incomplete fusion. When the laser beam oscillated in a sinusoidal path, the energy density on both sides of the amplitude was higher than the centerline, and the aspect ratio of the weld decreased. The speed of the beam along the centerline was found to be much higher than the speed on both sides of the amplitude. The molten pool oscillated in the width direction under the action of the oscillating beam, forming a concave surface, which promoted melting of the sidewalls of the groove and suppressed incomplete fusion defects in the sidewalls. The technical feasibility of NGHW assisted by laser beam oscillation was verified using a 60-mm-thick weld, which was characterized by a smooth layer transition and the absence of visible defects.

https://doi.org/10.29391/2022.101.014

Keywords

- High-Strength Low-Alloy (HSLA) Steel
- Narrow Groove Welding
- Hybrid Laser-Arc Welding
- Process Stability
- Droplet Transfer
- Laser Beam Oscillation

Introduction

Thick sections of high-strength low-alloy (HSLA) steel are widely used in ship manufacturing and bridge construction (Ref. 1). Narrow groove welding is one of the preferred techniques to reduce the groove cross-section area, improve welding efficiency, and reduce the heat input of thick welded sections. Currently, typical welding methods for narrow groove welding include gas metal arc welding (GMAW), gas tungsten arc welding, and submerged arc welding, particularly for the fabrication of sections with a thickness greater than 50 mm (Refs. 2–6). However, these methods suffer from unavoidable disadvantages such as large deformation, a wide heat-affected zone, high residual stress, and incomplete fusion.

The laser-arc hybrid welding (HLAW) technique has the best potential for welding thick and high-strength steel structures (Ref. 7). Carbon steel with a thickness ranging from 15 to 32 mm can be penetrated in one pass with a high-powered laser (Refs. 8–10). However, simply increasing the energy input using a high-powered laser does not appear to be an ideal technique for obtaining high-quality welds of thick structures.

In recent years, narrow groove laser welding (NGLW) has been significantly developed due to enhanced laser quality and the use of long focal-length converging focal systems (Refs. 12–15). Ensuring sufficient penetration in the groove

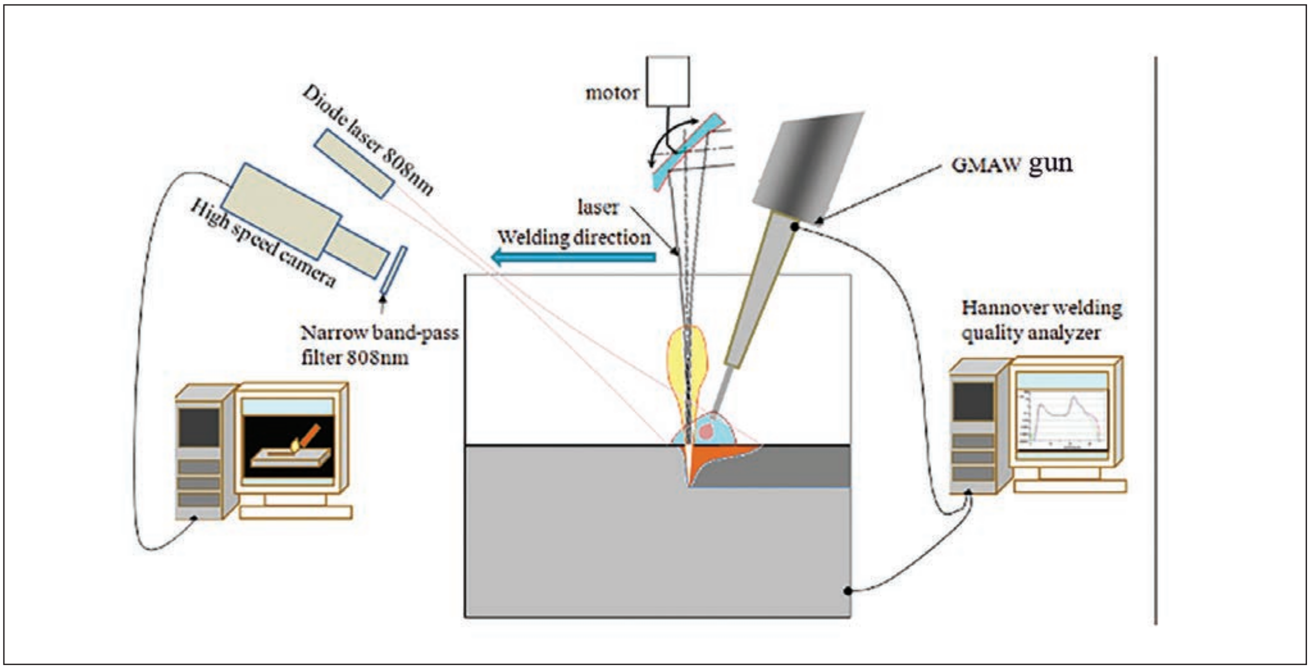

Fig. 1 — Schematic of the experimental NGHW setup.

sidewall is one of the main challenges for applying NGLW. In a related study, Tsukamoto et al. (Ref. 16) joined a 60-mm-thick SA516 low-carbon steel using multipass NGLW with a 10-kW fiber laser. Although the plate was welded in 10 passes, incomplete fusion was observed because the heat input was still low. Wang (Ref. 17) investigated NGLW of a 35-mm-thick Q345 mild steel and observed a small amount of incomplete fusion on the sidewalls. Studies have also demonstrated that groove preparation and beam-wire position are critical for thick sections (Refs. 18, 19).

Currently, beam oscillation, hot wire filling, and beam defocusing are the three main methods used to suppress incomplete fusion. For example, Yosuke et al. laser narrow groove welded a 50-mm-thick carbon steel by oscillating the laser beam at a high frequency (Refs. 16–18). By using a sensor during the process to recognize the groove shape, the heat input area was appropriately controlled and incomplete fusion was effectively prevented. Yosuke et al. (Ref. 20) butt joint welded 100-mm-thick SUS304 steel plates in an ultra-narrow groove using a laser with filler wire and more than 42 passes in the conduction mode, producing nearly defect-free welds. However, the incomplete fusion extent was not completely suppressed, and because small beams require high accuracy, the engineering applications of NGLW were restricted.

Narrow groove laser-arc hybrid welding (NGHW) is a recently developed technique that has the potential to suppress defects by combining the advantages of both laser and arc welding (Refs. 21–25). Laser-induced plasma, arc plasma, droplet transfer, and space constraints have been studied in detail in recent years. For example, Zhang et al. (Ref. 26) joined a 40-mm-thick mild steel using NGHW, and a defect-free joint was obtained using nine passes with a narrow groove 6 mm in width. Gong et al. (Ref. 27) quantified the effects of welding parameters on NGHW process stability

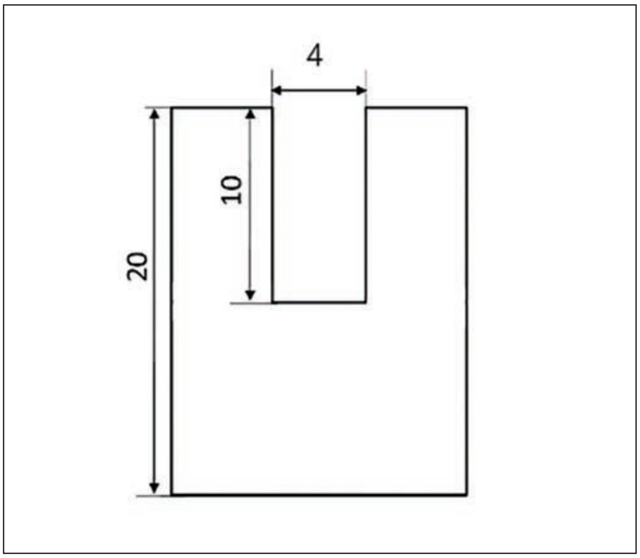

Fig. 2 — Dimensions of the narrow gap groove (mm).

using an approximate entropy method, thereby demonstrating the space constraint stabilization phenomenon caused by the narrow groove. In another study, Meng et al. (Ref. 28) explored the formation and suppression mechanism of incomplete fusion in NGHW with respect to the force and melt flow of the molten pool. These reported studies not only presented the tremendous potential of NGHW for the fabrication of thick plates but also revealed that the defects, such as incomplete fusion and porosity, can be easily identified in joints.

In this study, the authors proposed the use of an oscillated laser beam to suppress the incomplete fusion phenomenon

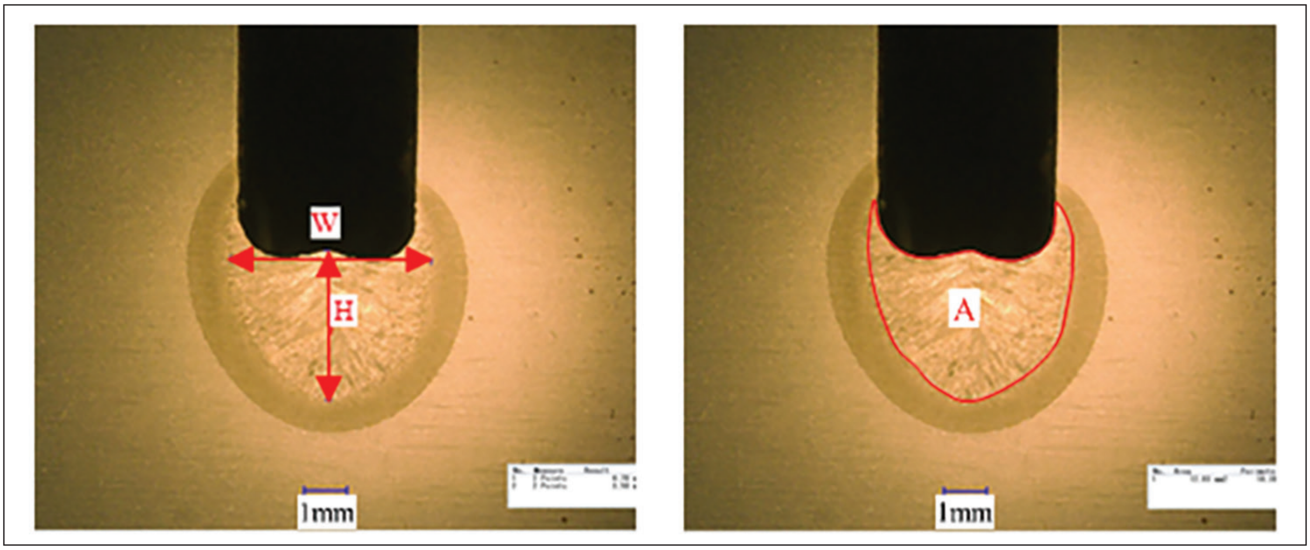

Fig. 3 — Dimensions of the weld cross-section sizes.

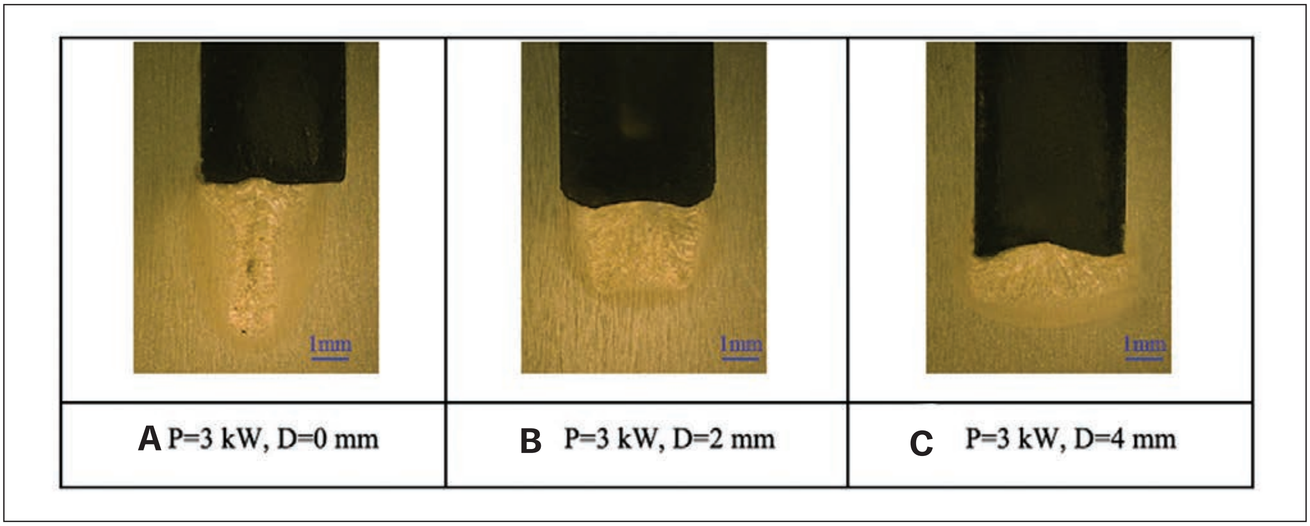

Fig. 4 — Weld cross sections for the different oscillating laser beams (V_f = 0 m/min).

Table 1 — Chemical Compositions of HSLA Steel and Filler Wire (wt-%)

	C	Si	Mn	P	S	Ni	Cr	Mo	V	Cu	Fe
Steel	0.14	0.22	0.99	0.005	0.006	1.38	1.04	0.39	0.04	0.05	Bal.
Wire	0.08	1.1	0.96	0.005	0.003	2.00	1.5	0.63	—	—	Bal.

and improve the process stability of NGHW. A sine-oscillating laser beam was used to improve the energy distribution of the molten pool and control the width of the weld. In addition, the molten pool was stirred to mitigate the challenges posed by the welding pores and unfused sidewalls. The results obtained in this study may be significant for the development of NGHW technology and its applications.

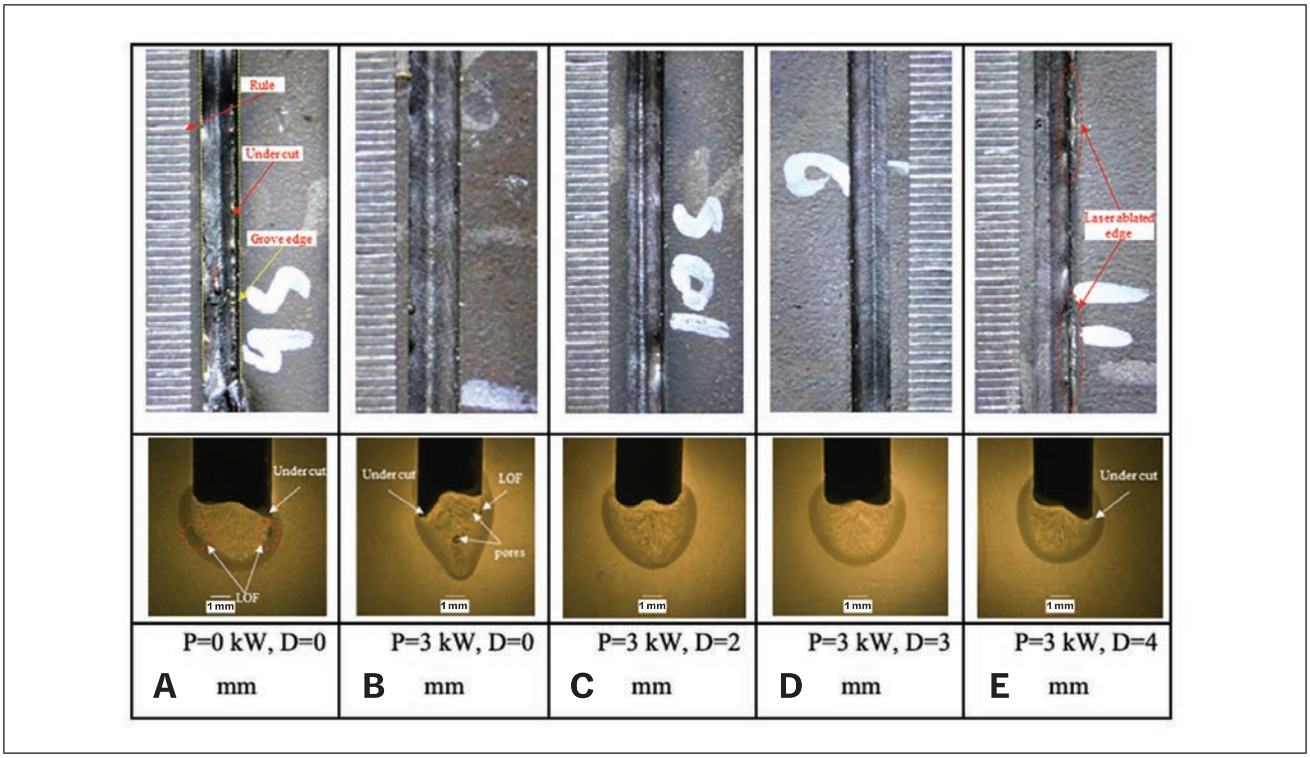

Fig. 5 — Weld appearance and cross sections under an oscillating laser beam (V_f = 10 m/min).

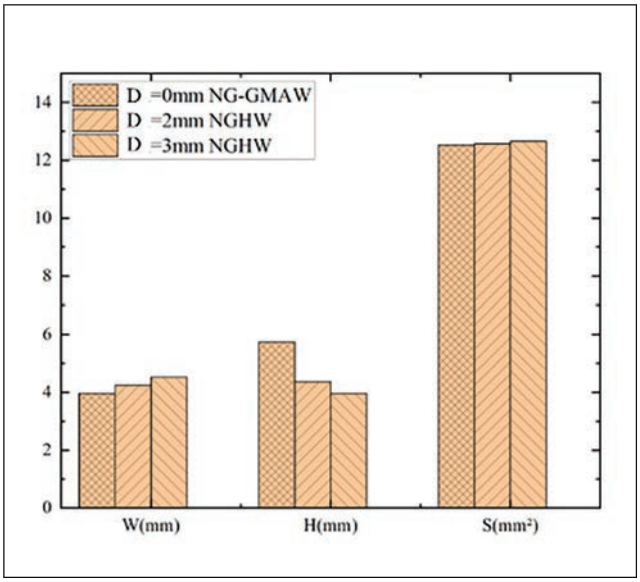

Fig. 6 — Comparison of the weld cross-section size.

Materials and Methods

HSLA steel plates, 20 and 60 mm thick, were used as the base material in this study in addition to low-carbon and high-toughness steel filler wire with a diameter of 1 mm. The chemical compositions of the base metal and filler wire are presented in Table 1. A mixed active shielding gas containing 95% argon and 5% carbon dioxide, was supplied at a flow rate of 30 L/min using an arc nozzle.

A continuous wave high-power fiber laser with a wavelength of 1070 nm and a beam parameter product of 13.8 mm·mrad was used in this work, where the power level of the laser used was 10 kW. A schematic of the experimental setup is shown in Fig. 1. The laser beam was transmitted through an optical fiber with a core diameter of 200 µm and was subsequently focused by a lens with a 300-mm focal length. A BIMO 1D scanner manufactured by HighYAG was used as the laser welding head. The laser light was oscillated in a defined wave by using a drive motor to control the angle of the scanner mirror inside the head. The laser beam could be oscillated in a defined wave by using a drive motor to control the angle of the scanner mirror inside the head. A 200-Hz oscillation frequency was taken in this study. The focal lengths of the collimation and converging lenses were 150 and 300 mm, respectively. A GMAW power source (TransPuls Synergic 5000, Fronius) was used as the second source, and a dedicated tooling was designed to simultaneously fix the laser head and GMAW gun on the manipulator. As a result, the two heat sources were coupled according to the set parameters during the welding process.

The laser was vertically irradiated on the specimen plate, where the angle between the filler wire and laser central axis was 30 deg, the distance between the laser beam central axis and the GMA electrode tip on the specimen surface was 2 mm, and the length of the filler wire from the GMAW nozzle to the workpiece was 17 mm. In this experiment, the focal point was set as right on the surface of the specimen; thus, the defocused distance was zero. The hybrid head was fixed on the axis of a KUKA KR 60 robot to ensure optimal mobility for orbital welding.

The welding processes were recorded using a high-speed imaging system, which was synchronized with a data acquisition system. A high-speed camera (V611, Photron) was used to obtain the arc shape and droplet transfer images. To suppress the arc light and obtain a shadowgraph of the droplets, an optical bandpass filter (808 ± 10 nm) and two polarizers were mounted in front of the camera lens. A diode laser with 40 W of power and a wavelength of 808 nm was used as the light source and placed on the same side of the high-speed camera. The sampling frequency was 5000 frames/s. The welding current, welding voltage, and short current frequency were measured with a Hannover welding quality analyzer at an acquisition rate of 5000 Hz.

Figure 2 shows the sample dimensions and size, where the thickness of the sample was 20 mm, the length was 100 mm, and the width was 40 mm. Additionally, the depth of the groove was 10 mm with a width of 4 mm. Table 2 presents the variations in welding parameters, such as the wire current, wire feed position, wire feed speed, and laser irradiation angle. After welding, the transverse cross section of the weld, 40 mm from the weld start, was etched with a 2% nital solution (2 mL of nitric acid mixed in 100 mL of ethanol) for 10 s. Then the cross section was observed by an optical metallographic microscope. Subsequently, the weld width (H), fusion zone area (A), and melting height of the narrow groove laser-arc hybrid weld were defined, as shown in Fig. 3. Based on the best process parameters for the 20-mm-thick sample, welding was carried out on a 60-mm-thick plate to verify the feasibility of NGHW for suppressing incomplete fusion.

Table 2 — Processing Parameters

Parameter	Variation Range	Parameter for 60-mm-Thick Sample
Laser power, *P* (kW)	3*	3*
Welding speed, *V* (m/min)	0.75*	0.5*
Wire feed speed, V_f (m/min)	10*	10*
Laser oscillation amplitude, *D* (mm)	0–4	3–4
Groove width, *G* (mm)	4*	4–6

*Indicates that the parameter was constant.

Results

Weld Shape Formation under an Oscillated Laser Beam

NGLW

The weld cross sections of the narrow groove laser welds under laser beams with different oscillating amplitudes are shown in Fig. 4 as well as Tables 3 and 4. Characteristic nail head shape penetration and pores appeared without an oscillated laser beam (D = 0 mm). As D increased from 0 to 4 mm, the heights of the welds decreased gradually and the widths of the welds gradually increased, thus exceeding the gap width (D = 0 mm). The aspect ratio of the welds decreased from 1.56 to 0.46. Furthermore, the weld cross section shown in Fig. 4C presented typical characteristics for thermal conduction welding.

NGHW

The weld appearance and cross sections of GMAW without laser power are presented in Fig. 5A, where the characteristic formations of defects associated with narrow groove welding were observed. The weld appearance and cross sections of NGHW without an oscillating laser beam (D = 0 mm) are presented in Fig. 5B, where characteristic nail head shape penetration was observed. Compared to GMAW, the welds obtained by NGHW without an oscillating laser beam (D = 0 mm) showed more forming defects. The weld shape formations as a function of the amplitude of the oscillating laser beam are illustrated in Figs. 5C and D, showing that the welds were well formed without any of the previously mentioned defects. The transition between the weld joint and the sidewall of the groove was also noted to be smooth. However, as the oscillation amplitude was equal to the groove width, as shown in Fig. 5E, the welding track deviated from the centerline of the groove. As a result, the laser was partially blocked by the edge of the groove, and defects such as undercut and incomplete fusion were observed. These challenges could be overcome by upgrading the laser transmission system or incorporating joint trackers. The influence of the oscillating laser beam amplitude on the weld cross-section size is illustrated in Fig. 6, which shows that as D increased from 0 to 3 mm, the H value decreased linearly and W increased. However, the laser was partially blocked by the groove edge; thus, a portion of the laser power could not reach the groove bottom.

Welding Stability under an Oscillating Laser Beam

Generally, the standard deviation of the welding current and welding voltage can be used to characterize the stability of the welding process. The dynamic welding current and voltage curves corresponding to Fig. 5 are presented in Fig. 7, where for all parameters, the typical short circuit transfer curves were observed. The magnitude of change in current and voltage between each metal transition decreased due

Table 3 — Weld Cross Section for the Different Oscillated Laser Beams (V_f = 0 m/min)

A P = 3 kW, LA = 0 mm	**B** P = 3 kW, LA = 2 mm	**C** P = 3 kW, LA = 4 mm

Table 4 — Weld Appearance and Cross Section under Oscillated Laser Beam (V_f = 10 m/min)

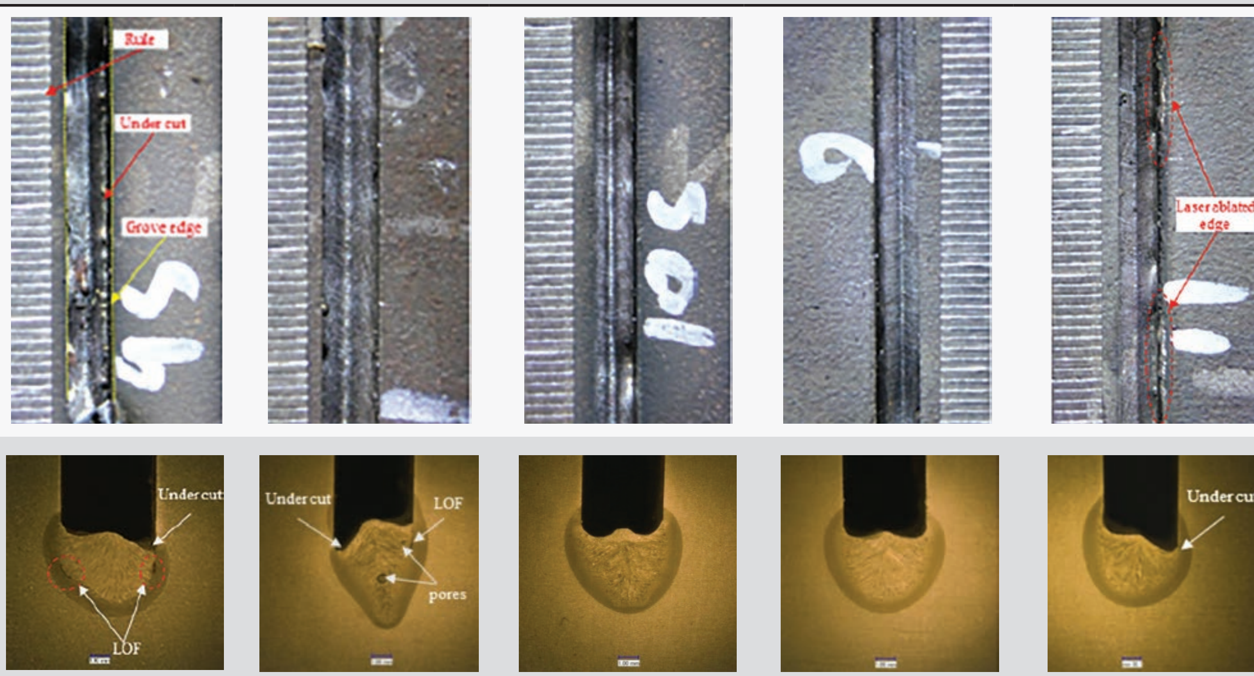

A P = 0 kW, LA = 0 mm	**B** P = 3 kW, LA = 0 mm	**C** P = 3 kW, LA = 2 mm	**D** P = 3 kW, LA = 3 mm	**E** P = 3 kW, LA = 4 mm

to the addition of the oscillating laser beam (D = 2, 3 mm), which resulted in better stability of the welding process.

Comparisons of the mean values and standard deviations of the welding current and voltage are illustrated in Fig. 8 (corresponding to Fig. 7), where the mean voltage and standard deviations were 18.4 and 5.3 V to 5.8 V, respectively. For narrow groove GMAW (NG-GMAW), the mean current and its standard deviations were 181.6 and 18.9 A, respectively. For NGHW, the mean current ranged from 184.8 to 186.2 A, with standard deviations of 26.4 to 28.8 A. Comparing NG-GMAW and NGHW, the laser power increased the welding current; however, there was no significant difference in welding voltage and its standard deviation. For NGHW with different D values, the mean values of the welding current and voltage did not show any significant changes; however, the standard deviation decreased as the D value increased from 0 to 3 mm. Thus, we inferred that when the oscillation amplitude D was in the range of 0 to 3 mm, welding stability improved due to the oscillating laser beam.

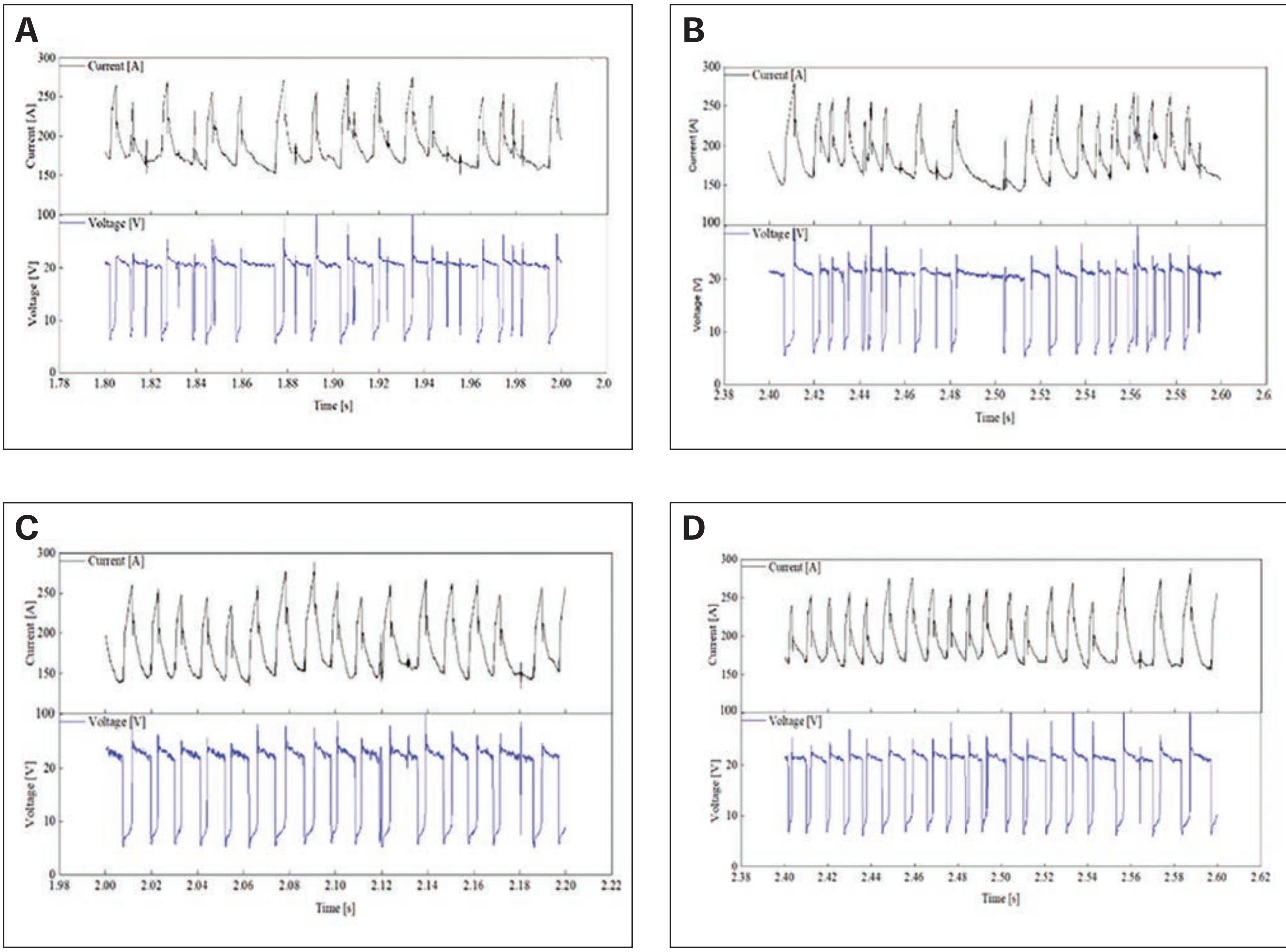

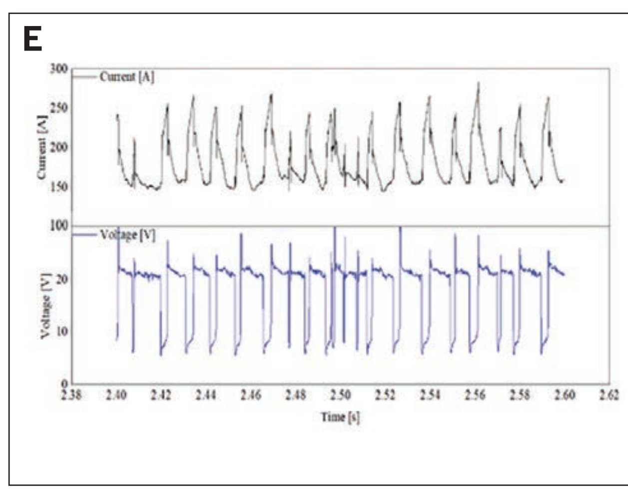

Fig. 7 — Dynamic welding current and voltage curves corresponding to Fig. 4: A — NG-GMAW; B — NGHW, P = 3 kW, D = 0 mm; C — NGHW, P = 3 kW, D = 2 mm; D — NGHW, P = 3 kW, D = 3 mm; E — NGHW, P = 3 kW, D = 4 mm.

Arc Behavior under an Oscillating Laser Beam

The arc behaviors of NG-GMAW without laser power are illustrated in Fig. 9, where the droplet transfer frequency was about 13 ms with an arc burning duration of about 9 ms. Typical high-speed images of arc behavior for various D values over time are presented in Figs. 9 and 10, which show that the use of a laser did not alter the droplet transfer mode and frequency; however, the arc burning duration tended to increase. The surface of the pool was noted as convex under the conditions used for NG-GMAW (Fig. 9) and NGHW without the oscillating laser beam (Fig. 10). Furthermore, the width of the weld pool was smaller than the groove gap. For the oscillating laser beam, the surface of the pool was noted to be concave, and the width of the weld pool was equal to the groove gap.

NGHW of 60-mm-Thick HSLA Steel Sections

In this section, we present an example application of NGHW with an oscillating laser beam for practical engineering. NGHW of a 60-mm-thick plate was carried out using the process parameters presented in Table 2. Figure 12A shows the groove geometry and sizes used during this process. For the back-

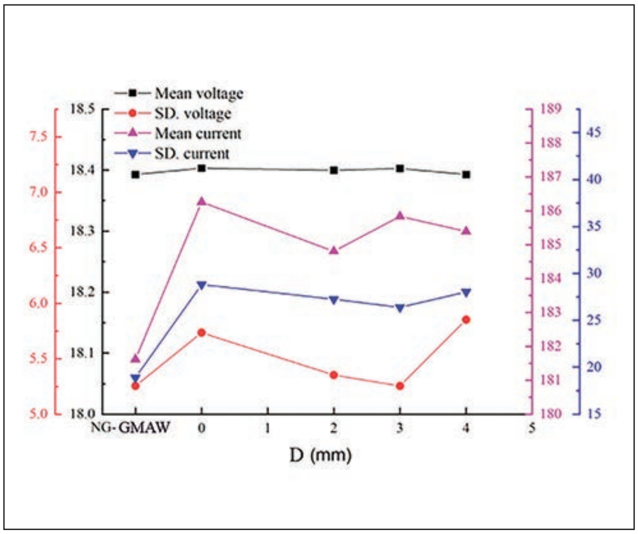

Fig. 8 — Comparison of the mean values and standard deviations of the welding current and voltage.

ing weld, an autogenous laser welding process was adopted using the following parameters: $v = 1$ m/min, $P = 4$ kW, and 0 mm positive defocusing. The NGHW processes were used to feed the welds, according to the parameters presented in Table 2. In addition, D was equal to the groove gap width at the welding position minus 1 mm. Of note, to avoid the influence of the groove sidewall on the oscillating laser beam, 2-mm positive defocusing was used during welding of the 60-mm-thick plate. According to the actual experimental results, this finetuning did not affect the welding process, possibly because the actual size of the laser spot did not change significantly during the process of adjusting defocusing from 0 to 2 mm.

After the welding process was complete, x-ray flaw detection and metallographic dissection were performed on the test piece. Figure 12B shows the cross-section profiles of the welded joints created with multilayer and single-pass NGHW. An acceptable weld was produced with 20 passes, and the weld did not show any visible defects and had a smooth transition between the passes. X-ray inspection results of the weld are shown in Fig.12C, which also showed no defects in the weld. Thus, an optimal weld bead without incomplete fusion and porosity could be produced with NGHW by using laser beam oscillation.

Discussion

Laser Energy Distribution under an Oscillating Laser Beam

A schematic diagram of NGHW is illustrated in Fig. 13, showing that the laser beam oscillated along the centerline of the gap. The sinusoidal path of the laser, its trajectory, and the velocity equation were expressed by Equations 1 and 2:

$$\begin{cases} X = v_w * t \\ Y = A\sin(2\pi F * t) \end{cases} \quad (1)$$

$$\begin{cases} v_x = v_w \\ v_y = 2\pi FA * cos(2\pi * F * t) \\ v_{xy} = \sqrt[2]{v_w{}^2 + [2\pi FA * cos(2\pi * F * t + \pi/2)]^2} \end{cases} . \quad (2)$$

Figure 14 shows the path and speed curves of the oscillating laser beam (D = 3 mm, $v_w = 12.5$ mm/s, and F = 300 Hz). When the laser was at both ends of the oscillating path, only the X-direction speed ($v_x = 12.5$ mm/s) was observed, which was also the minimum. When the laser was located at the center of the oscillating path, the X-direction speed (v_x) was 12.5 mm/s, whereas the Y-direction speed (v_y) was 2825 mm/s, which was 228 times v_x.

The average power density q_P can be defined as the ratio of the laser power P to the area of the laser spot on the surface A_s, as given by Equation 3:

$$q_P = \frac{P}{A_s} = 4P/(\pi d^2) \ [\mathrm{Wm^{-2}}] . \quad (3)$$

The interaction time defines the duration, during which a particular point is exposed to the laser beam while the beam moves in a sinusoidal path, as indicated in Fig. 15. Considering a point along the weld centerline, the interaction time τ_i for a circular beam with a diameter d traveling at a linear speed v_{xy} can be obtained by Equation 2, while a particular point exposed to the laser multiple times N_i can be obtained by Equation 5, depending on the distance from the weld centerline. The total interaction time τ is given by Equation 6:

$$\tau_i = d/v_{xy} \ [\mathrm{s}] \quad (4)$$

$$N_i = \frac{F*d}{v_w} , \quad (5)$$

$$\tau = \tau_i * N_i = F \cdot d^2/(v_w \cdot v_{xy}) \ [\mathrm{s}] . \quad (6)$$

The energy at a specific point E_{sp} is proportional to the product of the power density q_p, interaction time τ, and area of the laser spot on the surface A_s, as given by Equation 7.

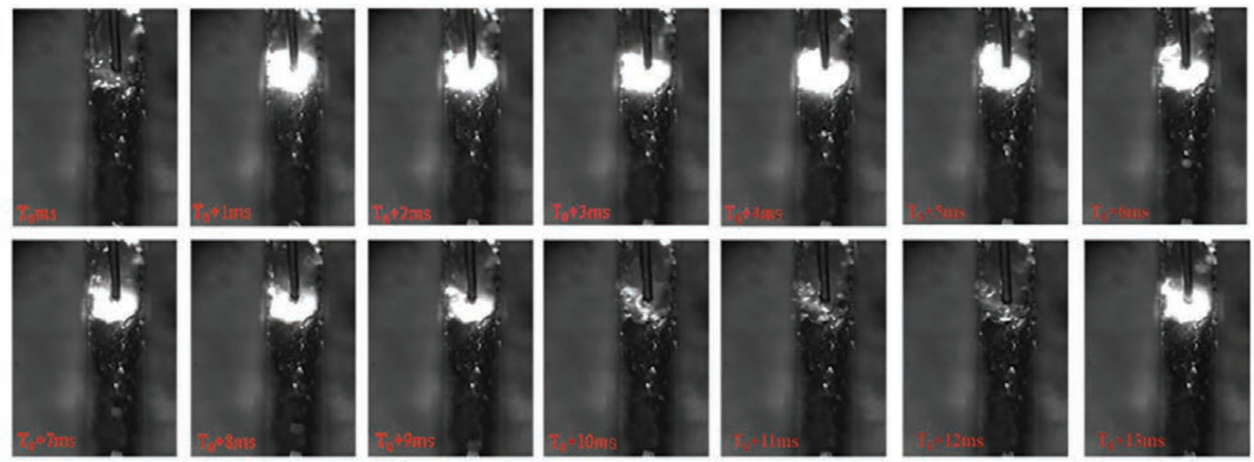

Fig. 9 — High-speed images of NG-GMAW.

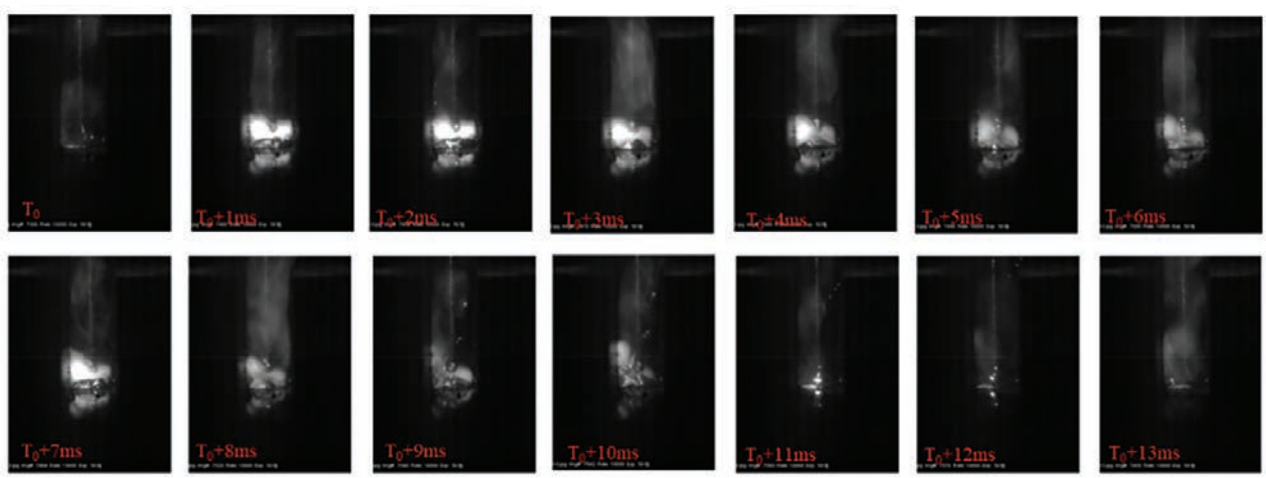

Fig. 10 — High-speed images of NG-GMAW (D = 0 mm).

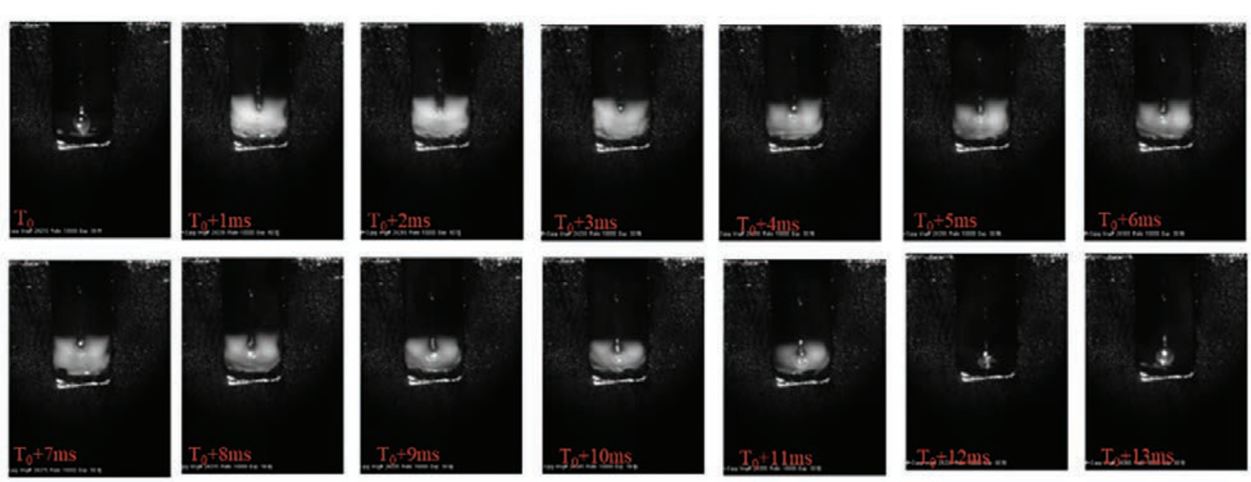

Fig. 11 — High-speed images of NGHW (D = 3 mm).

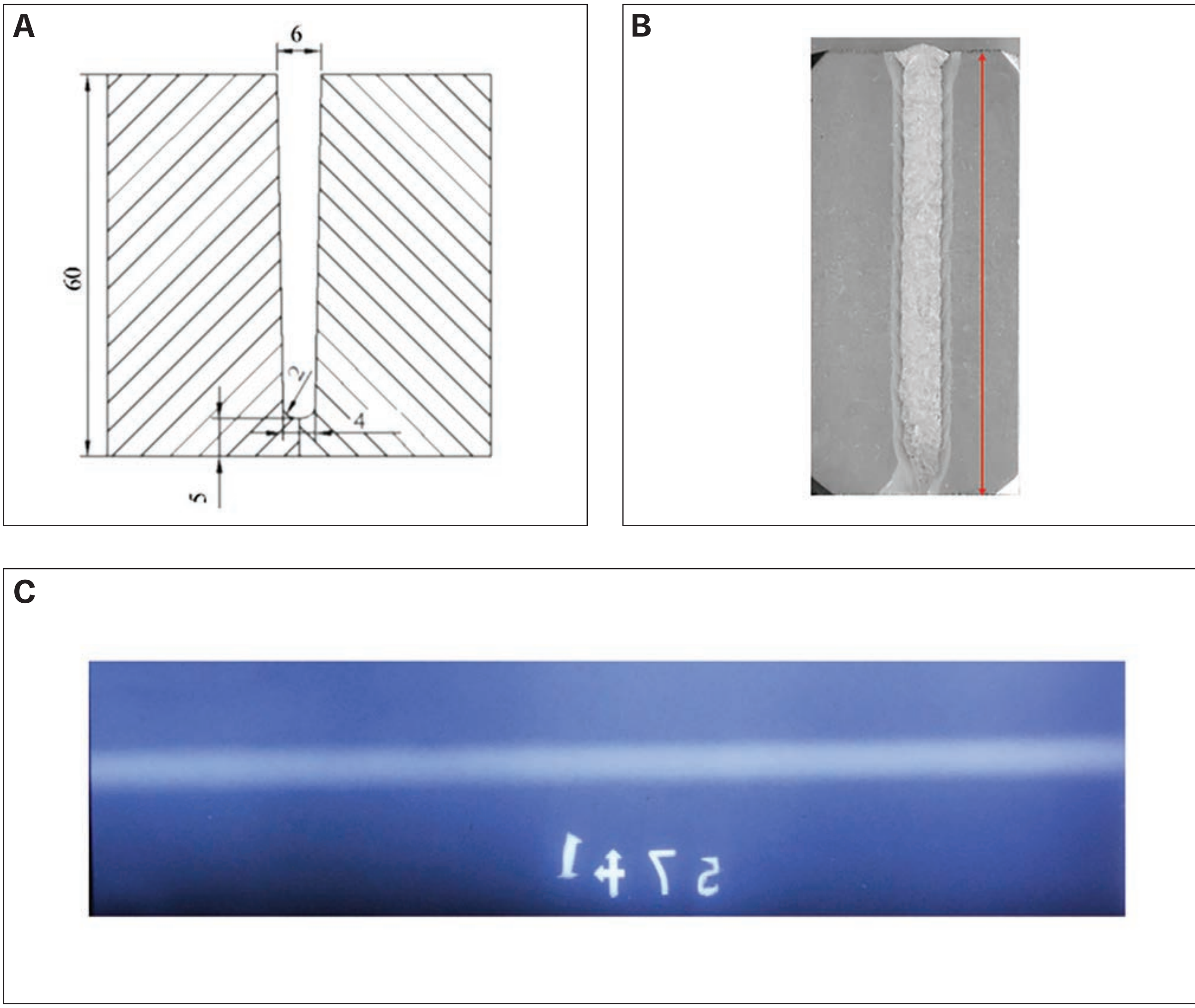

Fig. 12 — Cross section of the weld bead produced by NGHW using a 60-mm-thick plate: A — Groove geometry and sizes; B — cross section; C — x-ray inspection image.

$$E_{sp} = q_P * \tau * A_s = P * \tau = P * \tau_i * N_i = P \cdot F \cdot d^2/(v_w \cdot v_{xy})[\mathrm{J}] \ . \quad (7)$$

The laser energy distribution maps with and without the oscillating laser beam are shown in Fig. 16. We observed that the laser energy was distributed along the centerline without the oscillating laser beam. When the laser beam oscillated (D = 3 mm) the laser energy was distributed within a width of 3.4 mm, with the welding line acting as the axis of symmetry, depending on laser beam oscillation. As shown in Fig. 17, the peak energy input decreased geometrically; however, the interaction width increased significantly. Thus, the addition of the oscillating laser beam was beneficial for improving weld quality, which was mainly due to the change in energy input distribution. The width of the laser energy distribution increased, resulting in a wide and shallow weld instead of finger penetration. This was beneficial for the escape of gas during the solidification process, which reduced weld porosity. However, the high-energy density on both sides was conducive to ensuring the sufficient melting of the groove sidewall, which suppressed the formation of incomplete fusion defects due to the rapid heat dissipation of the groove sidewall.

Effect of the Oscillating Laser Beam on the Moving Mechanism of the Arc Attachment Point

NG-GMAW

Figure 18 shows the dynamic arc shape and arc attachment point (AAP) in NG-GMAW for V_f = 10 m/min. The arc was initially ignited between the wire tip and the molten pool and

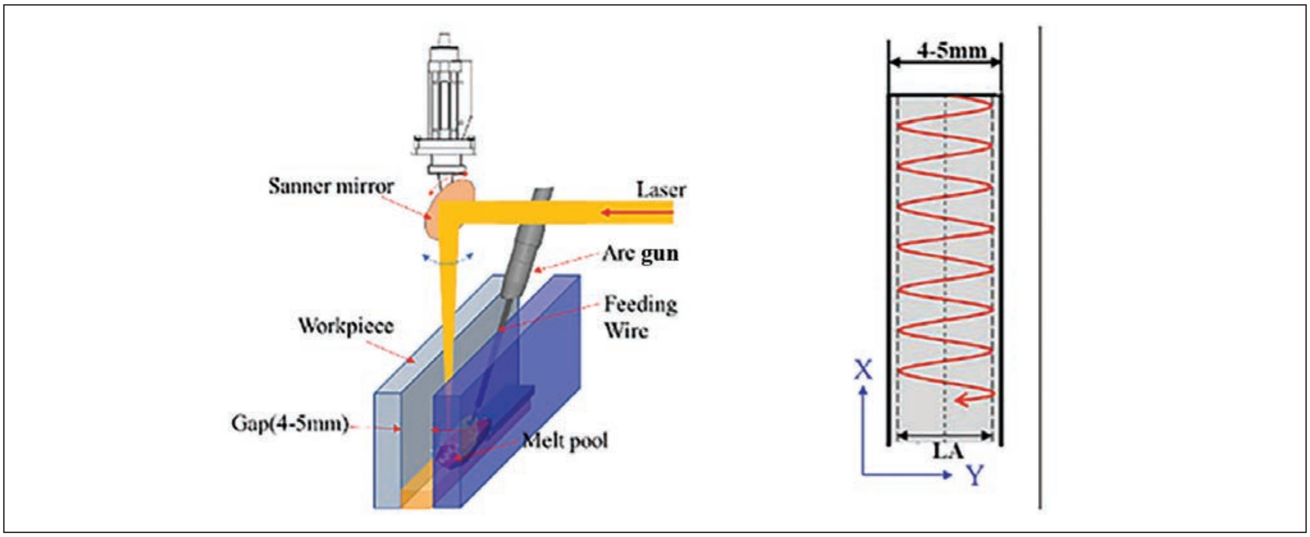

Fig. 13 — Schematic diagram of NGHW.

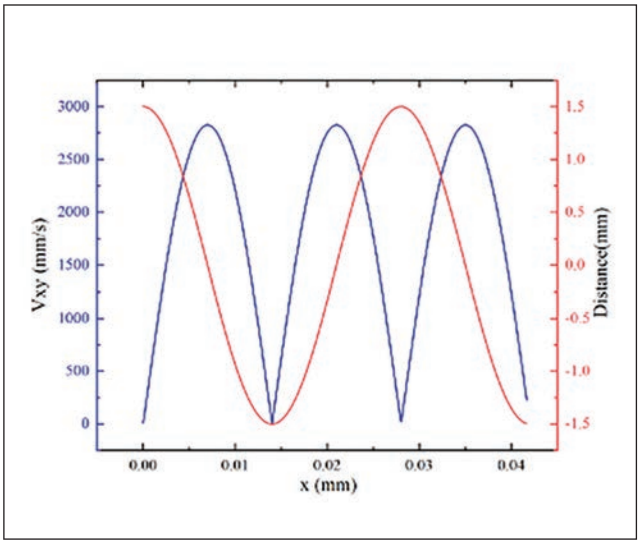

Fig. 14 — Path and speed curves of the oscillating laser beam (D = 3 mm, v_w = 12.5 mm/s, and F = 300 Hz).

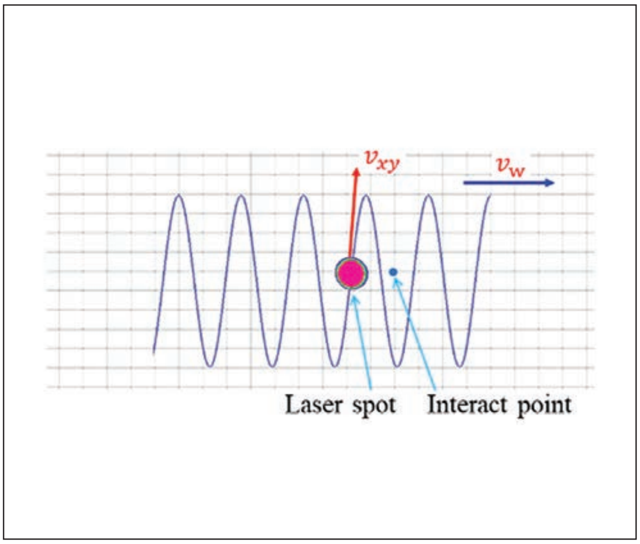

Fig. 15 — Interactions of the laser beam with the workpiece.

then climbed up the right sidewall. The arc burned between the wire tip and the right sidewall at $t = t_0 + 0.5$ ms. As the wire was continuously fed, the distance from the wire tip to the bottom of the gap was reduced by a similar distance from the wire tip to the right sidewall. At this stage, a new AAP was generated ($t = t_0 + 0.5$ ms), and the arc simultaneously burned among the wire tip, the right sidewall, and the bottom of the gap. At $t = t_0 + 11$ ms, the arc simultaneously burned among the wire tip, the sidewalls, and the bottom of the gap, resulting in the formation of three AAPs.

Based on the minimum arc voltage principle (Ref. 29), the burning arc will automatically identify an appropriate current path to ensure the minimum value of the electric field intensity in the arc column when welding parameters and other conditions are kept constant. Because the electrical field intensity of the arc exhibits a percentage ratio of the conductive path, the welding arc typically follows the shortest conductive path. Thus, the horizontal distance from the wire tip to the sidewall was shorter than the vertical distance of the wire tip to the molten pool on the bottom of the narrow groove, and AAP climbed up the closest sidewall, reducing the conductive path and maintaining a minimum arc voltage. The horizontal distance from the wire tip to the sidewall was similar to the vertical distance from the wire tip to the molten pool, and a new AAP was generated on the closest sidewall. After further feeding the wire, the horizontal distance from the wire tip to the sidewall became longer than the vertical distance from the wire tip to the bottom of the gap. As a result, the AAPs on the closest sidewall disappeared, reducing the conductive path and maintaining a minimum arc voltage.

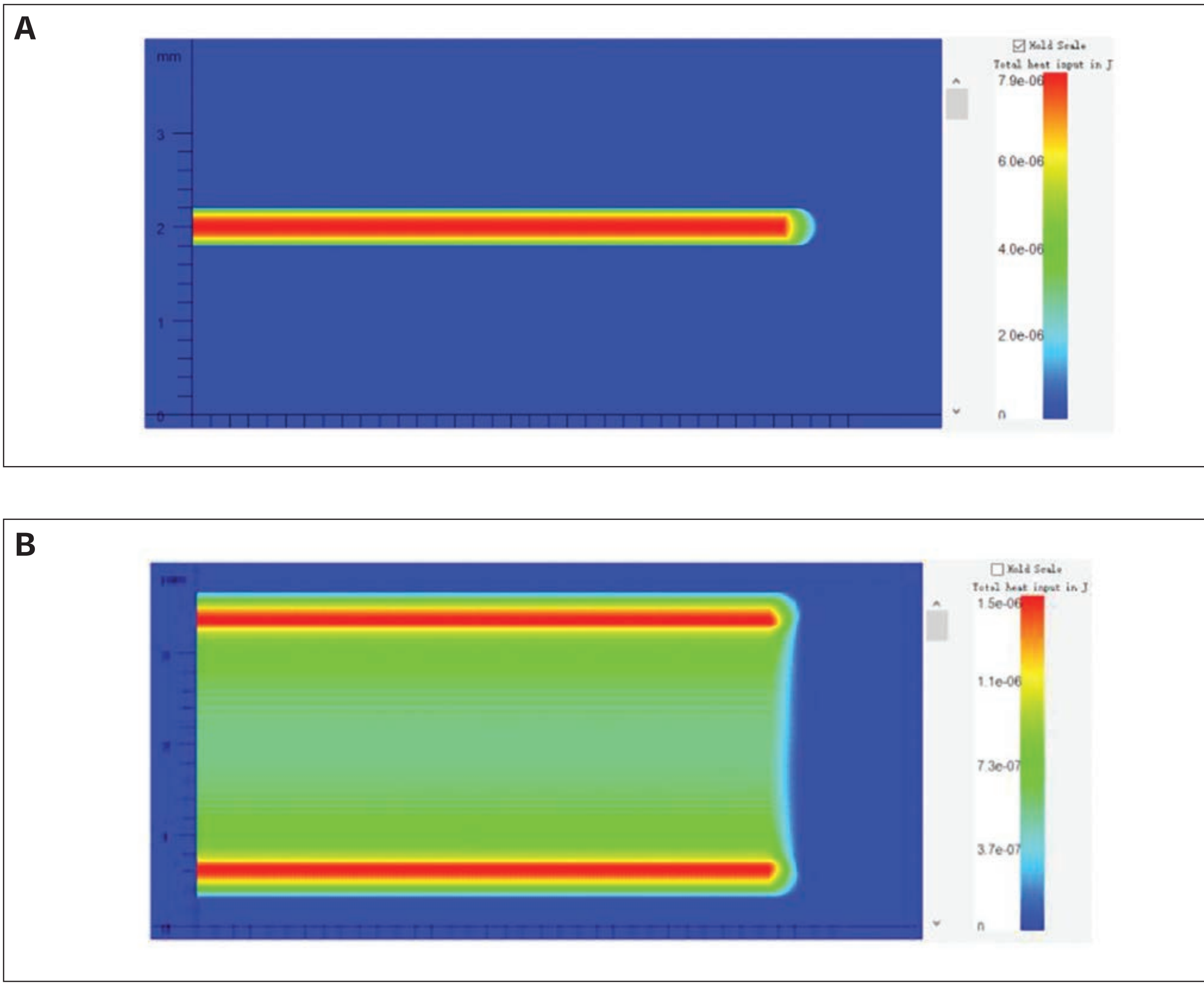

Fig. 16 — Laser energy distribution maps of the oscillating laser beam: A — D = 0 mm; B — D = 3 mm.

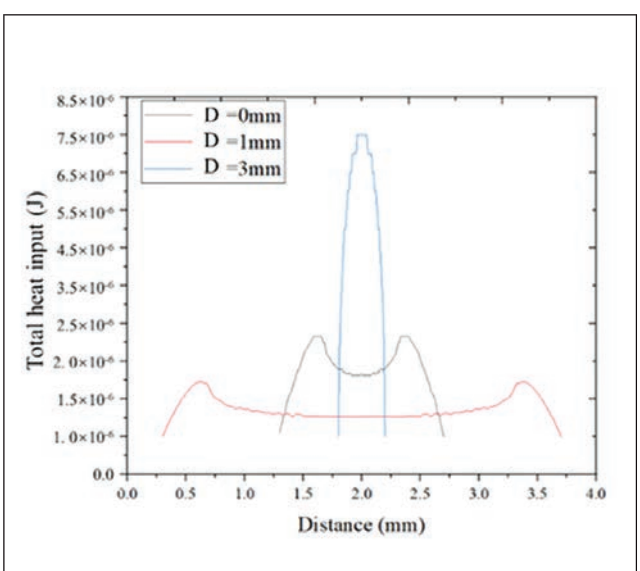

Fig. 17 — Laser energy distribution as a function of D.

NGHW

Figure 19 shows the AAP in NGHW for the oscillating laser beam (D = 4 mm). For the same GMAW parameters (Fig. 10), the arc initially ignited between the wire tip and molten pool (t_0 + 0.2 ms). Subsequently, the arc simultaneously burned between the wire tip and both sidewalls until the droplet touched the weld pool during NGHW (D = 3 mm). The distance from the wire tip to the molten pool was similar to the distance from the wire tip to both of the sidewalls.

The ionized state of the laser-induced metal vapor plume during welding using laser radiation with a wavelength of 1 µm was very weak (Refs. 30–32). Calculations of the ionization degree of iron and argon based on the Saha equation (Ref. 33) for the laser-induced metal vapor plume showed that it was weakly ionized, and the laser-induced metal vapor plume above the keyhole predominantly consisted of iron atoms. When the ionization voltage of iron atoms was 7.9 V, which was about half of the ionization voltage of the argon atoms (15.8 V) used as a shielding gas, the iron atoms were more easily ionized than argon. As a result, the laser-induced

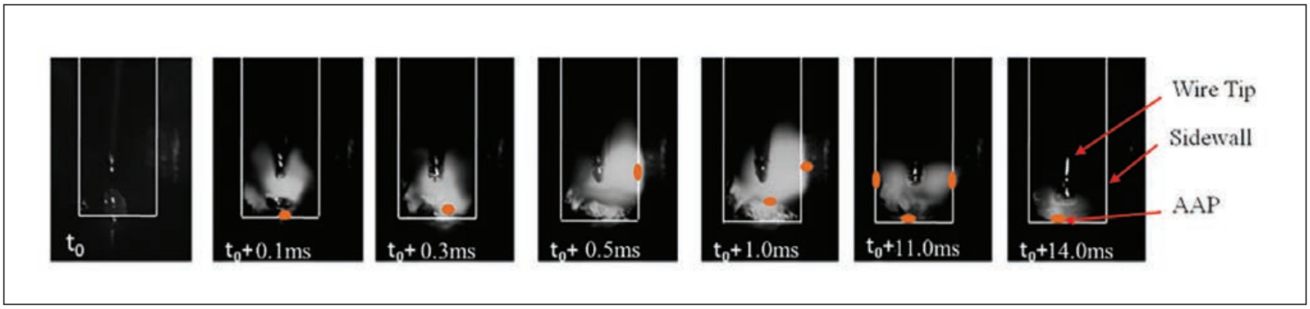

Fig. 18 — Typical images of the dynamic arc shape and AAP during NG-GMAW.

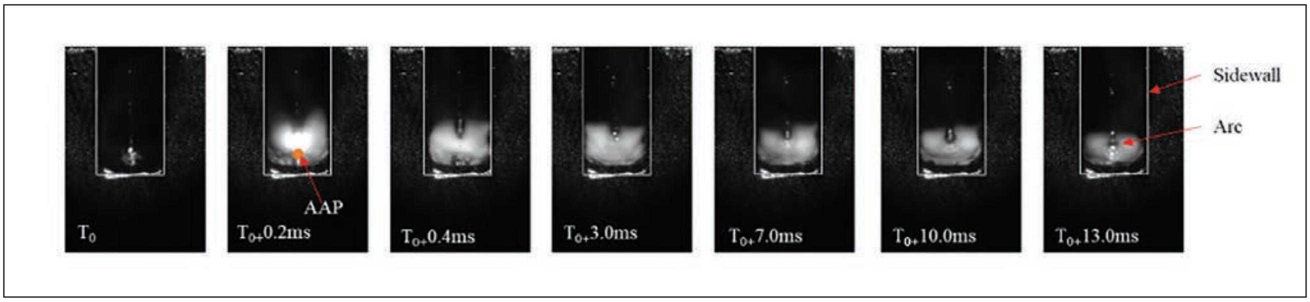

Fig. 19 — Typical images of the dynamic arc shape and AAP during NGHW (D = 3 mm).

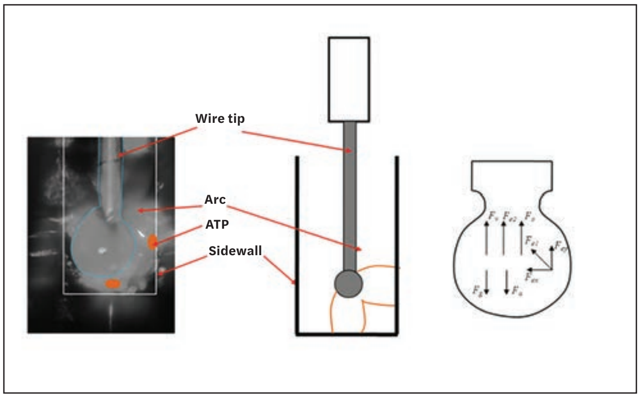

Fig. 20 — Simplified arc shape and forces acting on the droplet in NG-GMAW.

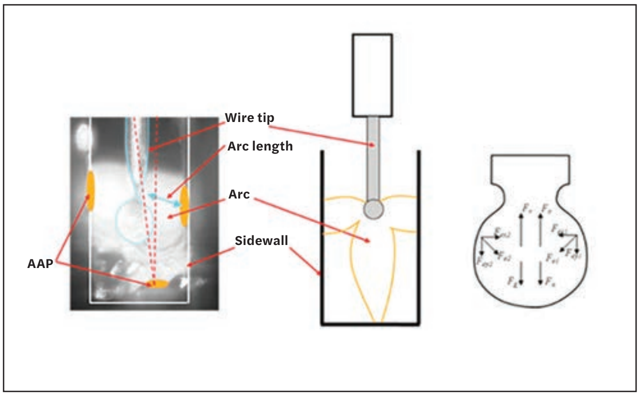

Fig. 21 — Simplified arc shape and forces acting on the droplet in NGHW (D = 3 mm).

metal vapor plume became the main source of electrons for the arc column. Consequently, it induced and stabilized the arc during NGHW by providing a stable cathode spot at the bottom of the gap. Thus, the authors of this research inferred that the laser-induced metal vapor plume above the keyhole was a concentrated source of electrons for the GMAW arc.

Metal Transfer and Suppression Mechanism of Incomplete Fusion

Metal Transfer Mechanism

The conventional static force balance theory (Refs. 34–36) was used to explain the metal transfer behavior in the NG-GMAW process. Figure 20 shows that the forces acting on the droplet included gravity F_g, surface tension F_σ, anode spot pressure F_v, plasma jet force F_α, and electromagnetic force F_e. The effect of F_e on the droplet transfer appeared to be complex due to the variations in AAP. When a small root area of the arc formed at the bottom of the droplet, the F_e acting on the droplet pointed upward, preventing droplet detachment from the wire tip. As a result, F_e gradually became an accelerating force, which promoted droplet detachment as the root area of the arc increased due to changes in the force direction. Based on the static force balance theory, it could be ascertained that the preventing force F_p combined with F_e, F_σ, and F_v was equal to the accelerating force $F_{\alpha c}$ combined with F_g and F_α, as expressed by Equation 8:

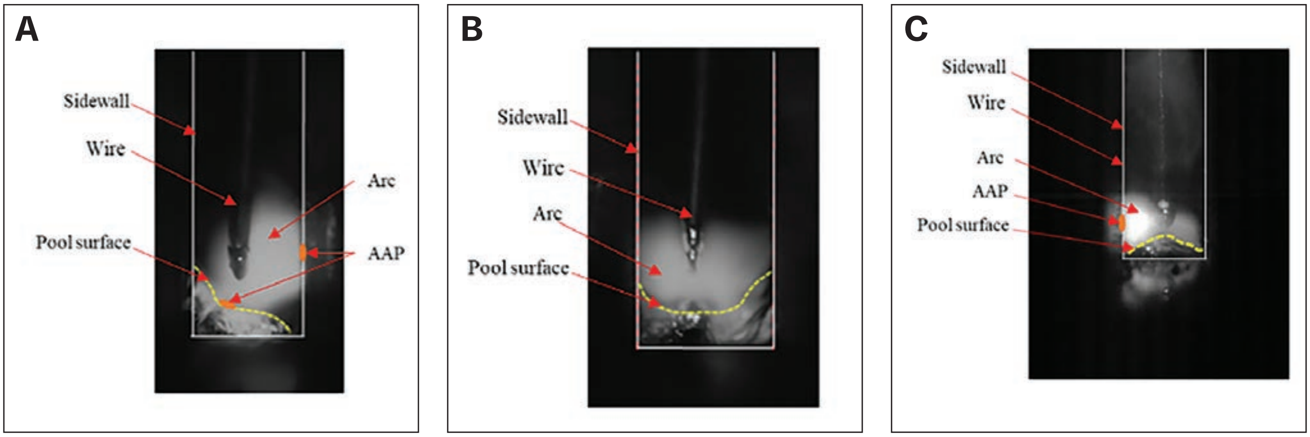

Fig. 22 — Typical images of the molten pool surface during different processes: A — NG-GMAW, V_f = 10 m/min; B — NGHW, V_f = 10 m/min, D = 3 mm; C — NGHW, V_f = 10 m/min, D = 0 mm.

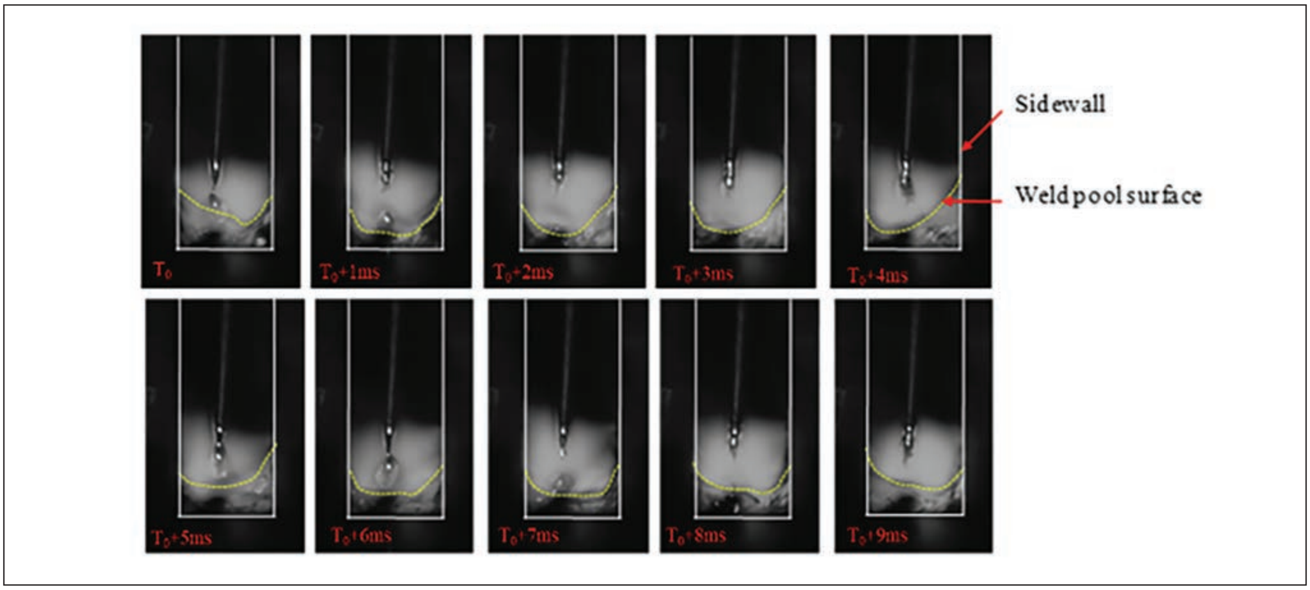

Fig. 23 — Typical effects of laser beam oscillation on the concave degree of the molten pool surface.

$$F_g + F_\alpha = F_\sigma + F_v + F_{ey} . \quad (8)$$

As shown in Figs. 9 and 10, the root area of the arc mainly acted on the lower half of the droplet, following the upward direction of F_{ey1} and F_{e2}, as illustrated in Fig. 21, thus preventing droplet detachment from the wire tip. Hence, the droplet detached as it contacted the molten pool, and the droplet transfer mode presented short current transfer.

As shown in Fig. 19, a symmetrically distributed arc was observed. Compared to the sideways arc in NG-GMAW, the distribution of F_e acting on the droplet changed. A schematic diagram of the process is presented in Fig. 21. The horizontal projections F_{ex1} and F_{ex2} of F_e accelerated the onset of necking due to their inverse actions. The two vertical projections of F_{ey1} and F_{ey2} enhanced the combination of electromagnetic forces in the axial direction and accelerated droplet detachment. The two arc conductive paths generated between the wire tip and sidewalls further increased the combination of force projections on the axial direction; thus, both the gravity and size of the droplet became smaller. This promoted droplet detachment from the wire tip with spray transfer mode.

Analysis of the Suppression Mechanism of Incomplete Fusion

Without a laser beam, and when the arc was the only heat source, the cathode spot moved randomly with oxides floating on the molten pool surface. When the groove width was narrow, the arc often climbed the sidewall due to its close proximity, as shown in Fig. 22A. At this time, energy input at the root of the groove decreased. Furthermore, as described in the metal transfer mechanism section, an asymmetrical arc usually caused the droplet to deflect to the other side. This further hindered the thermal melting of the groove root.

The combination of the above two aspects explained why incomplete fusion defects often appeared in NG-GMAW.

For NGHW (D = 3 mm), the energy distribution of the transversely oscillating laser resulted in a saddle shape (Fig. 17), which directly heated both sides of the groove bottom, as shown in Fig. 16B. The base metal melted by the laser created a leading molten pool in front of the arc. Due to CO_2 in the shielding gas, oxides were generated on the surface of the leading molten pool, which acted as cathodic spots that attracted subsequent arcs. As shown in Fig. 23, under the stirring action of the oscillating laser beam, the oxides on the leading molten pool were pushed to a position near the root of the groove on both sides. The subsequent arcs once again heated both groove roots under oxide attraction. Under the superposition of the two heating processes, the root of the groove was fully melted, which largely inhibited the generation of incomplete fusion. Moreover, the wide and shallow molten pool, which was caused by the increased width of laser energy distribution, filled the entire groove bottom. Thus, a concave surface eventually formed under the action of surface tension, as shown in Fig. 22B.

If the laser beam was always maintained at the center of the weld bead, following NGHW with D = 0, the arc would still be attracted by the oxides and follow the leading molten pool. As with the laser beam, the arc remained in the center of the weld. In this case, the arc was stabilized by the presence of the leading molten pool, which was similar to the oscillating laser beam. However, the energy input concentrated in the center of the weld bead created a deep, narrow weld pool. As a result, the surface of the molten pool was convex (Fig. 22C), the root of the sidewall could not be sufficiently melted, and the risk of incomplete fusion formation increased.

Conclusions

In this study, NGHW with an oscillating laser beam was conducted on HSLA steel plates. The effects of oscillation amplitude of the laser beam, as well as space constraints on the behavior, welding stability, droplet transfer, weld geometry, and incomplete fusion of the weld beads, were subsequently explored. The following conclusions were drawn:

1) The arc was significantly contracted by the sidewalls during narrow groove welding. Based on the minimum arc voltage principle and inherent arc self regulation, the stability of the arc shape during NG-GMAW and NGHW, without the oscillating laser beam, was poor. The arc attachment points reciprocated at the bottom of the narrow groove and sidewalls, resulting in insufficient energy to melt the root of the gap. The molten pool could not cover the entire width of the gap, resulting in the appearance of incomplete fusion defects. The laser-induced metal vapor plume above the keyhole acted as a concentrated source of electrons for the GMAW arc, thus prompting the melting of the wire and welding stability.

2) Under the experimental conditions, the laser beam oscillated in a sinusoidal path and the energy density range of the beam was dependent on the oscillation amplitude. The energy density on both sides of the amplitude was higher than the centerline. As the oscillation amplitude increased, the difference in laser energy density in the amplitude direction decreased. Furthermore, the aspect ratio of the weld declined, resulting in a wide and shallow weld.

3) The transversely oscillating laser will directly heat both sides of the groove bottom by changing its energy distribution. The base metal melted by the laser creates a leading molten pool in front of the arc. Oxides generated on the surface of the leading molten pool will act as cathodic spots to attract the subsequent arc. Under the stirring action of the oscillating laser beam, the oxides on the leading molten pool will be pushed to the position near the root of the groove on both sides. The subsequent arc once again heats both groove roots under the attraction of oxides. Under the superposition of the two heating processes, the root of the groove will be fully melted, which largely inhibits the generation of incomplete fusion.

4) In this work, an oscillation amplitude slightly smaller than the groove width was adopted to avoid the laser beam being disturbed. With the oscillating laser beam, the beam speed on the centerline was much higher than the speed on both sides of the amplitude. The molten pool oscillated in the width direction under the action of the oscillating beam, forming a concave surface, which promoted melting of the sidewalls of the groove and suppressed incomplete fusion defects of the sidewalls.

5) By controlling the oscillating amplitude of the laser beam, it was possible to effectively suppress incomplete fusion defects in the thick plates during NGHW. The technical feasibility of NGHW with laser beam oscillation was verified by 60-mm-thick welds, which exhibited a smooth layer transition and absence of any visible defects.

Acknowledgments

The authors would like to express their gratitude to the researchers who assisted with this study and Edit Springs (*editsprings.cn*) for the expert linguistic services provided.

References

1. Gomez, M., Valles, P., and Medina, S. F. 2011. Evolution of microstructure and precipitation state during thermomechanical processing of a X80 micro alloyed steel. *Materials Science and Engineering A* 528(13–14): 4761–4773. DOI: 10.1016/j.msea.2011.02.087

2. Massey, S. 2012. State-of-the-art in narrow groove welding technology and techniques. *Summary Report SR*. EWI.

3. Ning, J., Zhang, L. J., Yang, J., et al. 2019. Characteristics of multi-pass narrow-gap laser welding of D406A ultra-high strength steel. *Journal of Materials Processing Technology* 270: 168–181. DOI: 10.1016/j.jmatprotec.2019.02.026

4. Ribeiro, R. A., Assunção, P. D. C., et al. 2019. Application of cold wire gas metal arc welding for narrow gap welding (NGW) of high strength low alloy steel. *Welding, Joining and Coating of Metallic Materials* 12(3): 335. DOI: 10.3390/ma12030335

5. Liu, G., Tang, X., et al. 2020. Influence of interwire angle on undercutting formation and arc behavior in pulsed tandem narrow-gap GMAW. *Materials & Design* 193: 108795. DOI: 10.1016/j.matdes.2020.108795

6. Meng, Y., Li, G., Gao, M., et al. 2018. Effects of groove parameters on space constraint of narrow gap laser-arc hybrid welding. *Journal of Manufacturing Processes* 33: 144–149. DOI: 10.1016/j.jmapro.2018.05.006

7. Ribic, B., Palmer, T. A., and DebRoy, T. 2009. Problems and issues in laser-arc hybrid welding. *International Materials Reviews* 54: 223–244.

8. Gook, S., Gumenyuk, A., and Rethmeier, M. 2010. Weld seam formation and mechanical properties of girth welds performed with laser-GMA-hybrid process on pipes of grade X65. *Proceedings of the 29th International Congress on Applications of Lasers and Electro-Optics (ICALEO)*, 62–69. Anaheim, Calif. DOI: 10.2351/1.5062091

9. Bunaziv, I., Wenner, S., Ren, X., et al. 2020. Filler metal distribution and processing stability in laser-arc hybrid welding of thick HSLA steel. *Journal of Manufacturing Processes* 54: 228–239. DOI: 10.1016/j.jmapro.2020.02.048

10. Bunaziv, I., Akselsen, O. M., Frostevarg, J., et al. 2018. Laser-arc hybrid welding of thick HSLA steel. *Journal of Materials Processing Technology* 259: 75–87. DOI: 10.1016/j.jmatprotec.2018.04.019

11. Herbert, S. 2004. Laser-hybrid welding of ships. *Welding Journal* 83(6): 39–43.

12. Zhang, X., Ashida, E., and Tarasawa, S. 2010. Properties of welded joint for narrow gap laser welding of austenitic stainless steels. *Proceedings of the ICALEO 29th International Congress on Laser Materials Processing, Laser Microprocessing and Nanomanufacturing*, 632–637. DOI: 10.2351/1.5062092

13. Okagaito, T., Watanabe, H., Shinozaki, K. et al., 2012. Development of narrow gap hot-wire laser welding process for heat-resistant steel pipe for boiler. Preprint of the national meeting of Japan Welding Society, 91 (in Japanese).

14. Tsukamoto, T., Kawanaka, H., and Maeda, Y. 2011. Laser narrow gap welding of thick carbon steels using high brightness laser with beam oscillation. *ICALEO 2011 Congress Proceedings*, 141–146. DOI: 10.2351/1.5062227

15. Yamaguchi, K., Murai, Y., Eguchi, N., et al. 2011. Application of laser welding using band filler metal for narrow gap joint. Preprint of the national meeting of Japan Welding Society, 90 (in Japanese).

16. Tsukamoto, T., Kawanaka, H., and Maeda, Y. 2011. Laser narrow gap welding of thick carbon steels using high brightness laser with beam oscillation. *Proceedings of the 30th International Congress on Applications of Lasers and Electro-Optics (ICALEO)*, 141–146. Orlando, Fla. DOI: 10.2351/1.5062227

17. Wang, B. P. 2012. High-strength steel thick plate multichannel ultra narrow gap CO_2 laser welding with filler wire. Master's thesis, Shanghai Jiaotong University, Shanghai, China (in Chinese).

18. Nielsen, S., Hansen, L., and Kristensen, J. 1993. High power laser welding of C/Mn steel — The effects of using different filler materials and plasma control gases. *Proceedings of the 5th International Conference on Welding and Melting by Electron and Laser Beams*, 14–18. La Baule, France.

19. Salminen, A. 2010. The filler wire-laser beam interaction during laser welding with low alloyed steel filler wire. *Mechanika* 4(4): 67–74.

20. Yosuke, Y., Abe, Y., Hioki, Y., et al. 2014. Development of narrow gap multilayer welding process using oscillation laser beam. *Quarterly Journal of the Japan Welding Society* 32: 258–266 (in Japanese).

21. Yosuke, Y., Abe, Y., Hioki, Y., et al. 2014. Development of gap sensing system for narrow gap laser welding. *Quarterly Journal of the Japan Welding Society* 32(3): 122–129 (in Japanese). DOI: 10.2207/qjjws.32.122

22. Yosuke, Y., Abe, Y., Hioki, Y., et al. 2014. Fundamental study of narrow gap welding with oscillation laser beam. *Quarterly Journal of the Japan Welding Society* 32(2): 114–121 (in Japanese). DOI: 10.2207/qjjws.32.114

23. Wuxiong, Y., Jijun, X., Chao, F., et al. 2019. Microstructure and mechanical properties of ultra-narrow gap laser weld joint of 100 mm-thick SUS304 steel plates. *Journal of Materials Processing Tech.* 265: 130–137. DOI: 10.1016/j.jmatprotec.2018.10.017

24. Wang, P., Zuo, W. M., and Zhang, D. 2014. A compound pressure signal acquisition system for multichannel wrist pulse signal analysis. *IEEE Transactions on Instrumentation and Measurement* 63(6): 1556–1565. DOI: 10.1109/tim.2013.2267458

25. Wang, C. M., Zhang, C. M., Zou, J. Z., and Zhang, J. 2012. Performance evaluation for epileptic electroencephalogram detection by using Neyman-Pearson criteria and a support vector machine. *Physica A: Statistical Mechanics and its Applications* 391(4): 1602–1609. DOI: 10.1016/j.physa.2011.09.010

26. Zhang, C., Li, G., Gao, M., and Zeng, X. Y. 2017. Microstructure and mechanical properties of narrow gap laser-arc hybrid welded 40 mm thick mild steel. *Archives of Metallurgy and Materials* 61(2): 731–740. DOI: 10.3390/ma10020106

27. Gong, M. C., Kawahito, Y., Zeng, X. Y., et al. 2017. Stabilization effect of space constraint in narrow gap laser-arc hybrid welding analyzed by approximate entropy. *The International Journal of Advanced Manufacturing Technology* 92: 3093–3102. DOI: 10.1007/s00170-017-0354-6

28. Meng, Y. F., Li, G., Gao, M., et al. 2019. Formation and suppression mechanism of lack of fusion in narrow gap laser-arc hybrid welding. *The International Journal of Advanced Manufacturing Technology* 100: 2299–2309. DOI: 10.1007/s00170-018-2851-7

29. Lancaster, J. F. 1986. *The Physics of Welding* (second edition). UK: Pergamon.

30. Matsunawa, A., Kim, J. D., and Katayama, S. 1995. Spectroscopic studies on laser-induced plume of aluminum alloys. *Proceedings of International Congress on Applications of Lasers and Electro-Optics ICALEO*, 719–728. San Diego, Calif. DOI: 10.2351/1.5058976

31. Mueller, R. E., et al. 1999. Real time optical spectral monitoring of laser welding plumes. *Proceedings of International Congress on Applications of Lasers and Electro-Optics ICALEO*. San Diego, Calif.

32. Greses, J., et al. 2001. Spectroscopic studies of plume/plasma in different gas environments. *Proceedings of 20th International Congress on Applications of Lasers and Electro-Optics ICALEO*. Jacksonville, Fla. DOI: 10.2351/1.5059762

33. Zel'dovich, Y. B., and Raizer, Y. P. 1996. *Physics of Shock Waves and High-Temperature Hydrodynamic Phenomena*. New York (reprinted by Dover, 2002): Academic Press.

34. Amson, J. C. 1965. Lorentz force in the molten tip of an arc electrode. *British Journal of Applied Physics* 16: 1169–1179. DOI: 10.1088/0508-3443/16/8/316

35. Fan, H. G., and Kovacevic, R. 2004. A unified model of transport phenomena in gas metal arc welding including electrode, arc plasma and molten pool. *Journal of Physics D: Applied Physics* 37(18): 2531–2544. DOI: 10.1088/0022-3727/37/18/009

36. Haidar, J. 1998. An analysis of the formation of metal droplets in arc welding. *Journal of Physics D: Applied Physics* 31(10): 1233–1244. DOI: 10.1088/0022-3727/31/10/015

YANMING WU and **JIGUO SHAN** (*shanjg@tsinghua.edu.cn*) are with the Department of Mechanical Engineering, Tsinghua University, Beijing, China. **WU**, **ZHI LI**, **XINGHUA WANG**, **YAN FENG**, and **MINGLIN WANG** are with the Luoyang Ship Material Research Institute, Luoyang, China. **SHAN** is also with the Key Laboratory for Advanced Materials Processing Technology, Ministry of Education, Tsinghua University, Beijing, China.